Enhanced-Resolution Reconstruction of ASCAT Backscatter Measurements

Richard D. Lindsley, *Student Member, IEEE*, and David G. Long, *Fellow, IEEE*

***Abstract*—A wind scatterometer measures the normalized radar cross section σ° of the Earth's surface in order to estimate the ocean near-surface wind. Each measurement is the weighted integral of σ° over an area, so samples of σ° are filtered by a measurement spatial response function (SRF). Enhanced-resolution σ° data may be produced from σ° measurements and their associated SRF using image reconstruction algorithms. These enhanced-resolution data products are useful for land and ice studies in addition to high-resolution ocean wind retrieval. The spatial resolution and noise may be improved by combining data for multiple passes, trading off temporal resolution for spatial resolution. In this paper, we consider the production of enhanced-resolution σ° image reconstruction from the Advanced Scatterometer (ASCAT) on the MetOp satellites for land and ice regions. Two previously introduced image reconstruction algorithms, the weighted AVErage (AVE) and Scatterometer Image Reconstruction (SIR), are applied to ASCAT data, as well as a conventional gridding method. We select optimum values of the reconstruction parameters for ASCAT. The imaging algorithms are compared and evaluated, as quantified by the spatial resolution, pixel mean and variance, and pixel correlation of the produced images. The effective spatial resolution of the AVE and SIR reconstructed images is on the order of 15 to 20 km, an improvement over the nominal spatial resolution of 25 and 50 km for the spatially averaged swath-oriented ASCAT L1B products.**

***Index Terms*—Advanced Scatterometer (ASCAT), image reconstruction, radar remote sensing, scatterometer, spaceborne radar.**

I. INTRODUCTION

THE Advanced Scatterometer (ASCAT) on the MetOp series of satellites is a wind scatterometer that measures σ°, the Earth surface normalized radar backscatter. ASCAT data are primarily designed to retrieve vector winds over the ocean, but they are also valuable for other geoscience applications. These include mapping oil spills [1], measuring azimuth modulation over Antarctica [2], tracking icebergs, mapping sea ice [3], and measuring soil moisture content [4], among other land and ocean climate studies [5], [6].

Geoscience applications of scatterometer data can be limited by the relatively coarse spatial resolution of conventional processing techniques. The spatial resolution may be improved, however, with reconstruction techniques. The weighted AVErage (AVE) and Scatterometer Image Reconstruction (SIR) algorithms reconstruct the Earth surface σ° onto a high-resolution grid [7]. These algorithms have been applied to previous scatterometers, such as QuikSCAT [7], OSCAT [8], ERS [7], and NSCAT [9]. Applications of these reconstructed data include, among others, mapping and classifying sea ice [10], [11], melt detection of ice shelves [12], tracking and estimating icebergs [13], [14], mapping vegetation [15], [16], retrieving ocean vector winds at high resolution [17], and improved characterization of tropical cyclones [18].

The AVE and SIR reconstruction algorithms use the measurement spatial response function (SRF), i.e., the ground footprint imposed by the antenna pattern and onboard processing [7], [19]–[21]. The ASCAT measurement SRF is described in [22]. The SRF may be used for a single pass of data to reconstruct σ° for high-resolution wind retrieval, although resolution enhancement is limited. With multiple passes of data, the spatial resolution is improved at the expense of temporal resolution. Combining passes is best suited for temporally stable surfaces, such as land and ice. Additional reconstruction parameters, such as the choice of reconstruction pixel size, affect the reconstruction quality and computation time.

In this paper, we examine the enhanced-resolution ASCAT σ° reconstruction of land and ice. Enhanced-resolution ocean wind retrieval is discussed separately [23]. Considerations for enhanced-resolution processing of ASCAT data are discussed, including tradeoffs between resolution and noise. Section II contains background information on ASCAT as well as the image reconstruction algorithms used in this paper and their previous application to other scatterometers. The ideal resolution of the enhanced-resolution data is discussed in Section III, concluding with a discussion and selection of the image pixel size. We evaluate the impact of additional reconstruction parameters specific to ASCAT in Section IV. Section V demonstrates enhanced-resolution results for regions in Antarctica. The reconstruction statistics are evaluated in Section VI to quantify the accuracy and precision of the reconstructed data. A basic spectral analysis is also conducted to determine the effective resolution of the reconstructed data. Section VII concludes.

II. BACKGROUND

ASCAT, as with other wind scatterometers, is a radar that accurately measures σ°, the normalized radar cross section. Ground processing retrieves the ocean near-surface wind speed and direction from the σ° data. σ° data are also collected over land and ice for use in other applications.

Manuscript received August 3, 2015; revised September 26, 2015 and November 16, 2015; accepted November 18, 2015. Date of publication December 18, 2015; date of current version March 25, 2016.

The authors are with the Microwave Earth Remote Sensing Laboratory, Brigham Young University, Provo, UT 84602 USA (e-mail: rlindsley@mers.byu.edu; long@ee.byu.edu).

Color versions of one or more of the figures in this paper are available online at http://ieeexplore.ieee.org.

Digital Object Identifier 10.1109/TGRS.2015.2503762

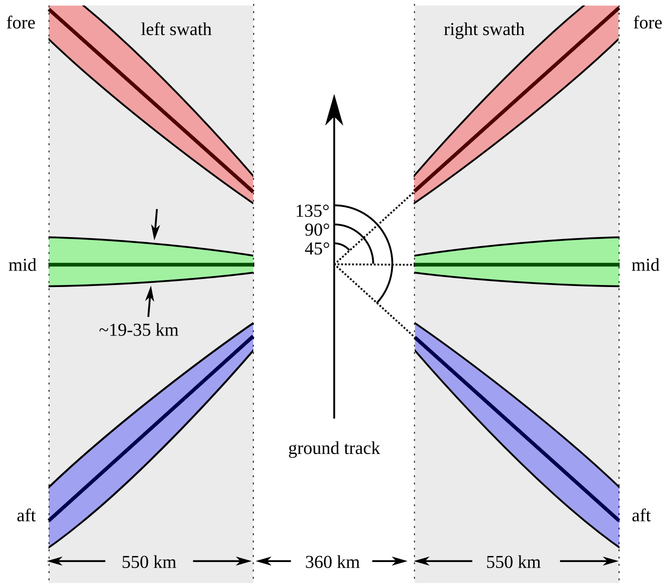

Fig. 1. ASCAT ground geometry. Both swaths are sampled at a range of incidence angles at azimuth angles fore, mid, and aft. Surface beamwidth is exaggerated for illustrative purposes.

ASCAT is a vertically polarized fan beam scatterometer operating at 5.255 GHz in the C band [5]. The ground geometry is illustrated in Fig. 1. Six beams—three for each of the two swaths—measure at azimuth angles fore, mid, and aft. Range-Doppler processing subdivides each fan beam into 256 measurements at varying incidence angles. The six beams are periodically calibrated to maintain high-quality σ° measurements in order to meet the requirements of wind retrieval.

An ASCAT instrument presently operates on each of the MetOp-A and MetOp-B satellites, launched in 2006 and 2012, respectively. The MetOp satellites are in a sun-synchronous near-polar orbit with a ground track repeat of 29 days [5].

ASCAT samples the Earth surface σ° over a distributed area filtered with an aperture function. Neglecting measurement noise, a σ° measurement can be expressed as

$$z_i = \frac{\iint \sigma^\circ(x,y) h_i(x,y)\, dxdy}{\iint h_i(x,y)\, dxdy} \tag{1}$$

where measurement z, index i, is the weighted combination of the surface $\sigma^\circ(x,y)$ and the SRF $h_i(x,y)$ for measurement i. The SRF represents the contribution from each location within the ground footprint and is a variable aperture function, i.e., the aperture function for each measurement may differ due to the sampling geometry. The SRFs are illustrated in Fig. 2 for two different measurements [22].

The measurement and observation geometry (radar backscatter, incidence angle, and azimuth angle) and location (in latitude and longitude) are reported for each measurement within each beam for the "full-resolution" (SZF) L1B product. Spatially averaged products (SZO, SZR) are also produced on a swath-oriented grid, where the value at each grid point is the combination of all nearby full-resolution measurements, spatially weighted with a Hamming window [5]. This paper does not consider the spatially averaged L1B products.

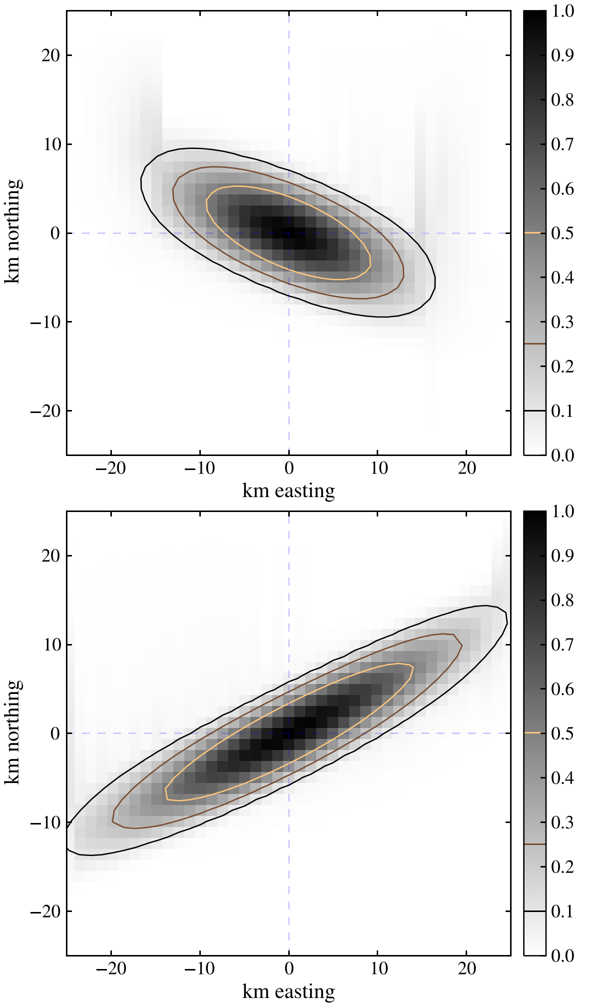

Fig. 2. Sample ASCAT SRFs with contours at 3, 6, and 10 dB below the peak. (Top) SRF from the right fore beam at 44° incidence angle. (Bottom) SRF from the left mid beam at 37° incidence angle.

For combining multiple passes of data, we use an Earth-located grid rather than a swath-oriented grid. On this Earth-located grid, the ASCAT measurements are irregularly spaced. Thus, the problem is to represent irregularly spaced aperture-filtered ASCAT measurements of σ° on a regular grid.

A traditional approach to dealing with irregularly spaced samples, referred to in this paper as the GRD method, is to define a uniformly sampled grid and use a "drop-in-the-bucket" approach to grid the measurements into a 2-D image of σ°. In this method, each grid element, or pixel, is the average of all measurement values (drops) whose centers fall within the pixel (bucket). Since the samples are irregularly spaced, a coarse resolution grid is required to reduce the number of pixels that do not contain any measurements as well as increase the number of measurements per pixel. Assuming uncorrelated measurement noise, averaging more measurements together reduces the noise for each GRD pixel. The effective resolution of the gridded data is the sum of the grid dimension and measurement spatial extent sizes. An alternative imaging method interpolates the measurements on a higher resolution grid. Since the measurements are noisy, the measurements are often averaged or filtered before interpolation to reduce the noise. Both approaches are effective in presenting the σ° samples as a spatial image but suffer from degraded spatial resolution.

Unlike the aforementioned approaches, image reconstruction retains the high-frequency information that is otherwise discarded, effectively performing a limited inversion of (1). The objective of reconstruction is to recover $\sigma^\circ(x, y)$—or, more precisely, the uniformly sampled version $\sigma^\circ[x_i, y_i]$—from multiple overlapping aperture-filtered measurements z_i in the presence of noise [21]. The AVE and SIR algorithms are two methods considered in this paper that reconstruct the Earth surface σ° field on a uniformly sampled high-resolution grid. Alternate reconstruction methods not considered here include the Backus–Gilbert inversion [24], [25] and a gradient method in Banach spaces proposed in [26].

The AVE and SIR algorithms have been applied to other scatterometers and radiometers, including QuikSCAT (1999–2009) [7], a long-running Ku-band pencil-beam scatterometer; OSCAT (2009–2014) [8], a scatterometer with similar design to QuikSCAT; and the scatterometers on ERS-1 (1992–1996) and ERS-2 (1996–2001) [7], a C-band scatterometer design previous to that of ASCAT. Enhanced-resolution data for these and other instruments are available online[1] as part of the NASA Scatterometer Climate Record Pathfinder project (SCP). The SCP data sets contain reconstructed high-resolution σ° imagery over many land and sea ice regions [27], [28].

For a collection of σ° measurements indexed by i, z_i, and a grid where j is the grid point, or pixel index, the AVE algorithm is

$$\sigma^\circ_{\text{ave},j} = \frac{\sum_i z_i h_{ij}}{\sum_i h_{ij}} \tag{2}$$

where h_{ij} is the SRF value $h_i(x, y)$ of measurement i sampled at pixel j. In effect, AVE is an average of all σ° measurements per pixel, weighted by the SRF value. The chief difference versus the GRD method is that the spatial extent of the measurement is defined by the SRF instead of treated as a point at the measurement center. Thus, each σ° measurement may affect multiple pixels instead of only one. This permits a finer resolution pixel grid than that used for GRD.

SIR is a modified algebraic reconstruction technique tuned for scatterometers and robust in the presence of noise [7]. The SIR algorithm is iterative with a nonlinear update term. The update term is weighted by the SRF similar to AVE

$$\sigma^\circ_{\text{sir},k,j} = \frac{\sum_i u^k_{ij} h_{ij}}{\sum_i h_{ij}} \tag{3}$$

where u^k_{ij} is the SIR update term for SIR iteration k, measurement i, and pixel j. The update term is

$$u^k_{ij} = \begin{cases} \left[\frac{1}{2p^k_i}\left(1 - \frac{1}{d^k_i}\right) + \frac{1}{a^k_j d^k_i}\right]^{-1} & d^k_i \geq 1 \\ \frac{1}{2}\, p^k_i \left(1 - d^k_i\right) + a^k_j d^k_i & d^k_i < 1 \end{cases} \tag{4}$$

where a^k_j is $\sigma^\circ_{\text{sir},k,j}$, pixel j of SIR iteration k; p^k_i is the forward projection of measurement i

$$p^k_i = \frac{\sum_j a^k_j h_{ij}}{\sum_j h_{ij}} \tag{5}$$

and d^k_i is a function of the σ° measurement z_i and the projection p^k_i

$$d^k_i = \sqrt{\frac{z_i}{p^k_i}}. \tag{6}$$

In effect, SIR inverts the SRF; it equalizes spatial frequencies distorted due to the SRF frequency response while reconstructing the irregular sampling defined by the measurement locations. However, the SIR algorithm is typically only used for a partial reconstruction since the number of iterations is truncated. Truncating the iterations is a form of regularization which reduces noise at the expense of spatial resolution. Further details on SIR may be found in [7] and [20].

The GRD method is similar to AVE, but the SRF h_{ij} is replaced with an indicator function G_{ij}, where $G_{ij} = 1$ if the center of measurement i falls within GRD pixel j and 0 elsewhere. GRD is therefore

$$\sigma^\circ_{\text{grd},j} = \frac{\sum_i z_i G_{ij}}{N_j} \tag{7}$$

since $N_j = \sum_i G_{ij}$ is the number of measurements in GRD pixel j. To maintain a large enough N_j, the GRD pixels are larger than those of AVE and SIR.

ASCAT measures σ° over a wide range of incidence angles θ. Over land and sea ice with incidence angles from about 30° to 60°, the dependence of σ° on θ can be modeled as a linear fit with σ° in a logarithmic space, such as dB:

$$\sigma^\circ(\theta) = \mathcal{A} + \mathcal{B}(\theta - 40^\circ). \tag{8}$$

In this model, σ° is decomposed into $\mathcal{A}$, which is the backscatter normalized to a 40° incidence angle, and $\mathcal{B}$, which describes the slope of the θ dependence [20], [27], [29], [30]. While any reference angle may be used, we use 40° to maintain consistency with SCP products from other scatterometers.

At the spatial resolution of ASCAT, most land regions are isotropic with respect to azimuth angle, whereas azimuth anisotropy is critical for ocean wind estimation. For land and sea ice applications of σ° data, σ° data from all azimuth angle directions are averaged together to increase the number of measurements available for reconstruction. For wind applications, each beam is separately reconstructed.

Data from multiple ASCAT orbits are used for enhanced-resolution processing over land and ice. Using multiple orbits of data over a few days increases the spatial coverage and improves the measurement density. Since the tradeoff is a reduced temporal resolution, using multiple passes is best suited for areas that do not rapidly change, such as land and ice.

A diagram of the sampling and reconstruction process is depicted in Fig. 3. The sampling process, including the measurement SRF used, is dictated by the instrument design and orbit geometry. The reconstruction process takes as input the

---

[1] http://scp.byu.edu

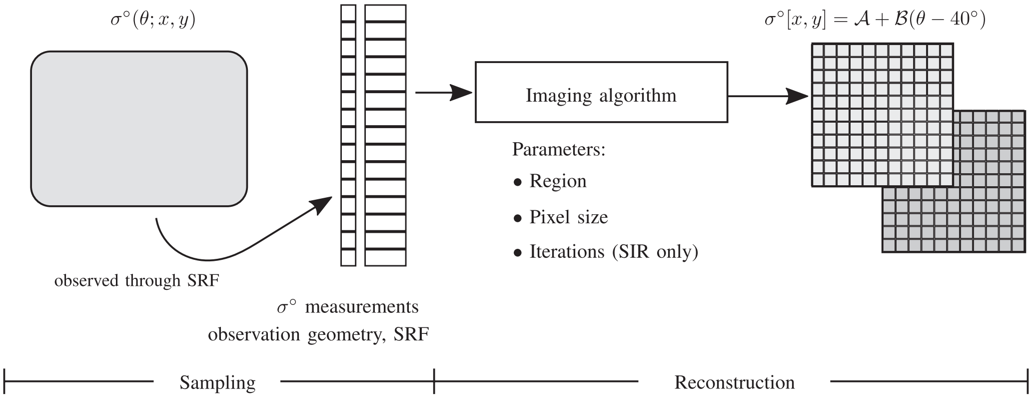

Fig. 3. Sampling and reconstruction process. The sampling process is already determined by instrument design and orbit geometry. For reconstruction, we represent $\sigma^\circ[x, y]$ from the ASCAT measurements, selecting parameters such as pixel size and reconstruction algorithm.

sampled σ° data and associated observation geometry and produces an output σ° image, shown here as decomposed into $\mathcal{A}[x, y]$ and $\mathcal{B}[x, y]$. This paper considers reconstruction parameters, including the choice of the image reconstruction algorithm and pixel size of the output image.

III. SPATIAL RESOLUTION

In this section, we examine the question of spatial resolution. As depicted in Fig. 3, image reconstruction operates on the irregularly sampled input data to produce a regularly sampled digital image. Both the input (ASCAT σ° measurements) and output (reconstructed σ° image) are samples of the same underlying signal—the Earth surface radar reflectivity $\sigma^\circ(x, y)$—but may have different notions of resolution.

Sampling theory dictates that, under approximate conditions, a band-limited signal may be sampled such that the samples completely represent the signal. The classic case of a band-limited, regularly sampled signal is governed by the Nyquist criterion—the samples perfectly represent the signal if the sampling frequency is at least twice the signal bandwidth.

Since the output σ° image is a regularly sampled signal, due to the Nyquist criterion, the spatial resolution of the image is at least twice the sample period, or pixel size. Thus, the output image has a *pixel resolution* determined from the pixel size. This differs from the *effective resolution*, which is determined by the input data and the reconstruction algorithm. To avoid aliasing, the pixel resolution must be equal to or finer than the effective resolution. For simplicity, we use square pixels so that the pixel resolution in the x-direction is the same as in the y-direction.

An important component to enhanced-resolution processing is the choice of pixel size for the output image. Choosing a smaller pixel size increases the storage requirements and computation time of the image reconstruction. A smaller pixel size than is necessary provides no benefit to the image effective resolution. Choosing a larger pixel size leads to aliasing of the signal and a loss of effective resolution. Since the image reconstruction also evaluates the measurement SRF on the pixel grid [h_{ij} in (2) and (3)], an additional constraint is that the pixel size adequately samples the SRF values. Thus, the choice of pixel size is motivated by computational cost and SRF quantization, in addition to the effective resolution of the image.

The image reconstruction algorithm ideally preserves the effective resolution of the input data. It is difficult to exactly quantify the effective resolution of ASCAT σ° data. The frequency response of the underlying σ° signal, the sampling geometry, and the measurement SRF all may affect the effective resolution.

Because the input data consists of irregularly sampled aperture-filtered measurements, the conditions of classic sampling theory are too restrictive for ASCAT and other scatterometers. It has been shown [7], [31] that, analogous to the Nyquist criterion

$$T_s < \frac{1}{2B} \tag{9}$$

for a signal band limited to $[-B, B]$ and sampled regularly with period T_s, an irregularly sampled signal with frequency extent $[-B, B]$ must satisfy

$$\delta < \frac{\ln 2}{2B} \tag{10}$$

in order to be fully represented by its samples. The parameter δ is the maximum sample spacing. A spatial region is said to be δ-dense if the union of all rectangles with width δ centered on each measurement completely fills the region [31].

Whatever the true band limit of the signal, given irregular samples with a density of δ, (10) dictates the recoverable band limit. The signal, if band limited, may or may not be aliased. If the signal is not band limited, then it is certainly aliased. A band-limited signal implies that the signal has infinite extent in the spatial domain. Since the true σ° signal is finite in extent, it cannot be purely band limited. However, we treat it as *approximately* band limited.

We justify treating σ° as approximately band limited due to its behavior: Radar reflectivity is a physical process with a power-law relationship that results in a red spectrum, i.e., the power density is inversely proportional to frequency. Although the true σ° signal has high-frequency content that is aliased due to sampling, the energy in this portion is minimal for a suitably chosen sample frequency. Additionally, since the

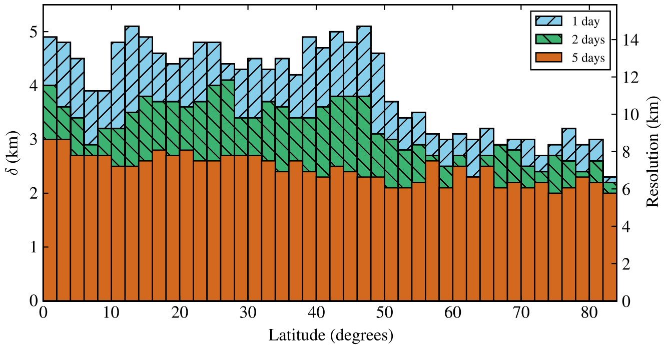

Fig. 4. Sample density δ as a function of latitude for bins of latitude using 1, 2, and 5 days of ASCAT data. The smallest spatial resolution that may be reconstructed is also indicated.

aperture functions that sample the σ° signal are generally low pass, this further suppresses the high-frequency energy so that the aliased energy can be ignored. We note that, because of the filtered or ignored high-frequency content, the reconstructed enhanced-resolution image is a band-limited version of the true continuous signal $\sigma^\circ(x, y)$.

We thus treat (10) as satisfied for the available sampling, i.e., the σ° samples have a δ-density sufficiently large to represent the σ° signal band limited to B, as determined by (10). In order for the pixels of the output image to represent this band-limited signal, (9) must be satisfied. Since we assume that (10) is satisfied, we combine them to yield

$$T_s < \frac{\delta}{\ln 2}. \tag{11}$$

This represents the largest pixel size T_s that can represent the band-limited signal, which is irregularly sampled at a density of δ. Since (11) implies no aliasing of the irregularly sampled signal, the effective resolution is the same as (or more coarse than) the pixel resolution. As stated earlier, the pixel resolution is $2T_s$. Thus, from (11), the best case effective resolution may be computed directly from δ: $2\delta/\ln 2$.

The parameter δ is intrinsic to the observation geometry and sample spacing. A simple estimate for δ is found by binning the measurements over a region at various grid sizes. The smallest grid size with no empty bins is the estimated δ. For ASCAT, using only one azimuth look from a single pass of data yields the largest nominal δ: approximately 5.25 km. From this single-pass single-beam δ, the worst case effective resolution is therefore 15.15 km. Combining all beams and using multiple passes reduce δ, but this is a function of latitude: Due to the near-polar orbit, locations at high latitudes are sampled more densely than those closer to the equator. The density δ and effective resolution are shown in Fig. 4 as a function of latitude using 1, 2, and 5 days of data. The average δ for equatorial and polar regions is displayed in Table I. The theoretical spatial resolution that may be reconstructed in these cases is also shown.

TABLE I
AVERAGE δ AND CORRESPONDING SPATIAL RESOLUTION FROM FIG. 4 FOR EQUATORIAL (< 50°) AND POLAR (> 55°) LATITUDES

	Equatorial latitudes		Polar latitudes	
Days	δ (km)	Resolution (km)	δ (km)	Resolution (km)
1	4.6	13.3	3.0	8.5
2	3.6	10.3	2.6	7.4
5	2.6	7.5	2.2	6.4

For compatibility with existing SCP data sets, we choose a pixel size of $8.9/2 = 4.45$ km. In order to avoid aliasing, this pixel size is selected since it is slightly smaller than the pixel sizes of 4.6 or 5.6 km required to represent 9.2- or 11.5-km resolution data from the 5- or 2-day δ values.

As part of AVE and SIR reconstruction, the SRF is quantized or sampled on the same grid used to reconstruct the σ° data. The chosen pixel size of 4.45 km is on the order of the width of a measurement SRF. While this coarse quantization of an SRF is not a particularly accurate representation of the SRF, no issues are apparent in the final reconstruction output using this coarse representation over a more finely quantized version using a smaller pixel size.

For comparison purposes in this paper, we also consider a reconstruction pixel size of 3.125 km for a pixel resolution of 6.25 km. To match the resolution of the spatially averaged ASCAT data, which are produced at 25- and 50-km resolution [32], we create conventionally gridded σ° images on a grid spacing of 12.5 and 25 km for pixel resolutions of 25 and 50 km. The alternate pixel size of 3.125 km for the reconstructed images permits an easier comparison between the gridded versus the reconstructed images since the gridded pixel sizes are an integer multiple of the reconstructed pixel size.

IV. RECONSTRUCTION PARAMETERS

We consider three reconstruction parameters for ASCAT: 1) the pixel size; 2) the number of SIR iterations; and 3) the quantization of the SRF estimate. The choice of pixel size, or posting grid, is discussed earlier in Section III. In this section, we evaluate the other two parameters.

Since SIR is an iterative algorithm, the number of SIR iterations is a parameter that affects the final reconstruction output. This parameter controls a tradeoff between the image fidelity and the noise added or amplified during the reconstruction process. Prematurely terminating the SIR iterations is a regularization that results in a partial reconstruction but reduces noise. The number of iterations can be fixed or chosen dynamically, e.g., by terminating if the change in image values as a function of iteration falls below some threshold. Here, we select a fixed value for the number of iterations.

The SRF may be quantized in order to reduce computation. The quantized, or binary-valued, SRF is an approximation to the true, or full-valued, SRF $h_i(x, y)$, which is 1 inside the SRF 3-dB contour and 0 outside. A quantized SRF was previously used for QuikSCAT slice measurements to reduce computational complexity [19]. We evaluate this approach for the ASCAT SRF by reconstructing with both the original SRF and the quantized SRF.

We use simulations to select both the number of SIR iterations and choose between a full-valued or binary-valued SRF by minimizing the error metrics defined hereinafter. A synthetic "truth" image of $\sigma^\circ[x, y]$ is created and sampled using ASCAT measurement geometry and the full-valued SRF estimate. Discretizing the sampling process as described by (1), the synthetic ASCAT measurement σ_i° is expressed as

$$\sigma_i^\circ = \frac{\sum_j \sigma^\circ_{\text{true},j} h_{ij}}{\sum_j h_{ij}} \tag{12}$$

where j indexes the pixels of the true σ° image, i indexes the measurements, and h_{ij} is the full-valued SRF value of measurement i at pixel j.

Measurement noise is additionally simulated. A multiplicative model for scatterometer measurement noise often adopted [33] is

$$z_i = \sigma_i^\circ (1 + K_{p,i}\, \nu_i) \tag{13}$$

where z_i is the σ_i° affected by measurement noise, $K_{p,i}$ is a per-measurement noise term, and ν_i is a zero-mean unit-variance uncorrelated Gaussian random process. The noisy measurements z_i are distributed as

$$z_i \sim \mathcal{N}\left(\sigma_i^\circ, (K_{p,i}\, \sigma_i^\circ)^2\right). \tag{14}$$

Both noisy and noise-free samples of the synthetic image are processed using AVE and SIR reconstruction as well as the traditional GRD method ("drop-in-the-bucket"). AVE and SIR are produced at a grid spacing of 3.125 km, and GRD is produced at grid spacings of 12.5 and 25 km. Reconstruction is performed using either full-valued or binary-valued SRF estimates and for various iterations of SIR. The reconstruction error is quantified by the evaluation of the difference between the reconstructed $\widehat{\sigma^\circ}[x, y]$ results and the input synthetic image $\sigma^\circ[x, y]$.

For this section, we define the *signal error* as the standard deviation of the difference between the synthetic truth image and the reconstructed output when using noise-free samples. It is the difference between the actual scene and the reconstructed scene in the ideal sense, i.e., with no measurement noise. We also define the *noise error* as the standard deviation of the difference between reconstruction outputs when using noise-free versus noisy synthetic measurements. This represents the error due only to the measurement noise. As SIR iterates, the reconstruction amplifies the noise error as it reduces the signal error. The objective of the simulation is to find an optimum number of SIR iterations such that these two error metrics are jointly minimized, as well as to evaluate the effect of SRF quantization on the signal and noise errors [7].

A parametric plot of signal error and noise error as a function of SIR iteration is shown in Fig. 5 for a particular truth image using the full-valued and the binary-valued SRF to reconstruct. Since the partial reconstruction process is not a linear operation, the error values depend on the truth image chosen. However, the general trend is similar among the various truth images evaluated: The first few iterations of SIR rapidly reduce the signal error at the expense of additional noise. After about ten iterations, the signal error continues to decrease, but the increase in noise error is less dramatic. After about 30 iterations, any further reduction in signal error is small, but noise error continues to slowly increase. The decrease in signal error indicates resolution enhancement via improved signal reconstruction.

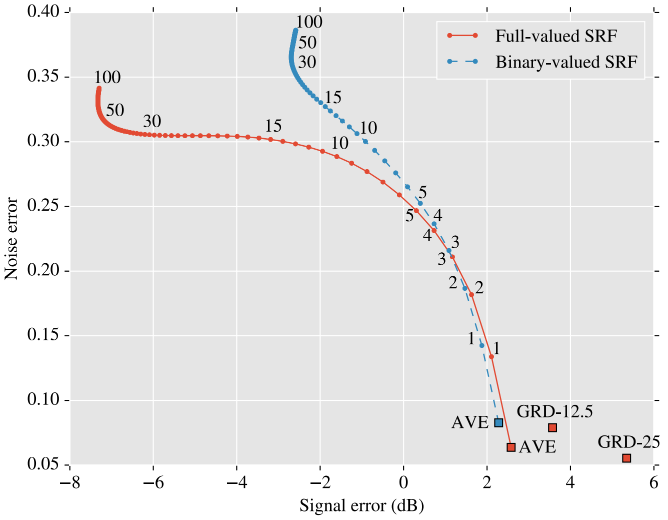

Fig. 5. Noise error versus signal error for a synthetic truth image for up to 100 SIR iterations. The solid line indicates reconstruction with the full-valued SRF, and the dashed line indicates reconstruction with the binary-valued SRF. Selected iterations of SIR are labeled along with AVE and GRD.

With the quantized SRF, AVE has a slightly lower signal error but larger signal error than with the original SRF. However, as SIR iterates, the full-valued SRF permits a greater reduction in signal than the binary-valued SRF. Although exact values vary as a function of input truth image, the trend is similar for all cases tested: A quantized SRF may improve AVE, but it limits the performance of SIR.

The error for GRD at both grid spacings is also shown in Fig. 5. The noise error is very low, but the signal error is larger than that for AVE or SIR. This illustrates an important tradeoff in enhanced-resolution image reconstruction: The signal error is improved at the expense of greater noise. In some applications, the improved spatial resolution may not justify the additional noise, but for other applications, this tradeoff is acceptable.

Based on the simulation results, we use the original SRF for reconstruction and select 30 iterations of SIR. Additionally, the SCP data sets contain ASCAT images using the AVE and GRD algorithms to allow users some control over the noise/resolution tradeoff.

V. RECONSTRUCTION RESULTS

To illustrate the effectiveness of resolution enhancement, examples of conventional images using gridding and enhanced-resolution images using AVE and SIR are shown in this section. The gridded images are produced at pixel sizes of 12.5 and 25 km using the GRD method (referred to as GRD-12.5 and GRD-25, respectively), and the AVE and SIR images are produced at a pixel size of 3.125 km. We use the reconstruction parameters selected in Section IV: 30 iterations of SIR using the full-valued SRF.

Two regions of Antarctica, shown in Fig. 6, are selected as study regions. Because ASCAT is in a near-polar orbit, only

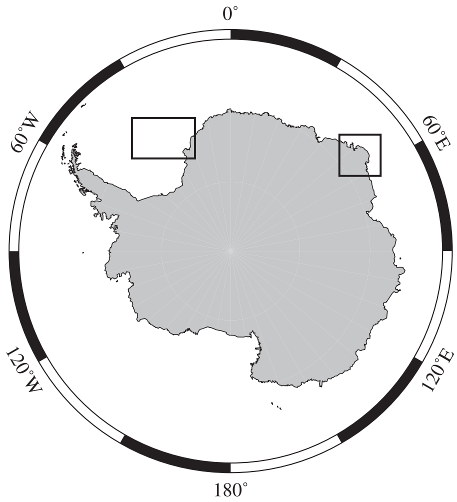

Fig. 6. Regions of Antarctica used for Figs. 7 and 8. Fig. 7 contains the Weddell Sea (left box), and Fig. 8 contains Enderby Land (right box).

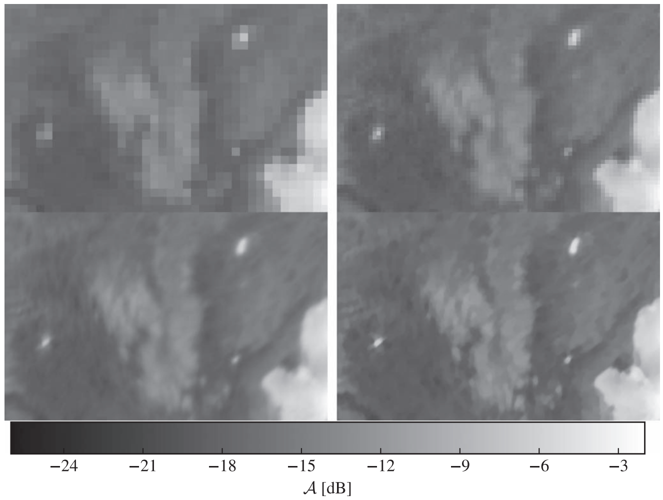

Fig. 7. $\mathcal{A}$ images of a region from the Weddell Sea, Antarctica. Top left: Gridded with a pixel spacing of 25 km, Top right: Gridded at 12.5 km. Bottom left: AVE at 3.125 km. Bottom right: SIR at 3.125 km after 30 iterations.

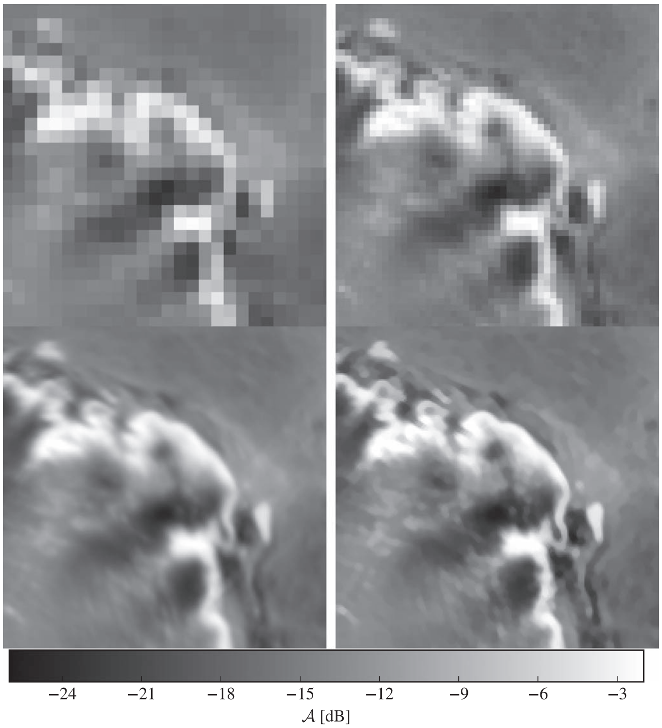

Fig. 8. $\mathcal{A}$ images of a region from Enderby Land, Antarctica. Top left: Gridded with a pixel spacing of 25 km. Top right: Gridded at 12.5 km. Bottom left: AVE at 3.125 km. Bottom right: SIR at 3.125 km after 30 iterations.

nine orbits (about 15 h) are required to completely sample the land area. Sea ice extent varies as a function of time, but we find that two days of data is a good compromise between complete land and sea ice coverage and high temporal resolution.

Figs. 7 and 8 show the reconstructed images for both regions. Two days of data (299–300, 2011) are used, with $\mathcal{A}$ (incidence angle-normalized σ°) images shown. Fig. 7 shows the Weddell Sea, with the Brunt Ice Shelf visible on the right edge. Most of the region consists of sea ice, with some icebergs visible as brighter patches. Many features are visible in all four images, but the iceberg shape and orientation are more defined in the AVE and SIR images compared to the GRD images. The smaller grid spacing of the GRD-12.5 image is an improvement over the larger spacing in the GRD-25 image, and AVE and SIR further improve on the GRD-12.5 image. SIR is similar to AVE, but the contrast between sea ice and iceberg or ice shelves is sharpened. In effect, SIR deblurs the AVE data.

Fig. 8 contains part of Enderby Land and shows icebergs visible in the top left and center right of the region. The coarse grid spacing of the GRD-25 precludes the recovery of any small-scale features. With GRD-12.5, some smaller features become visible; with AVE, the size and shape of icebergs and the coastline are more clear. SIR sharpens the transition between contrasting features, such as the icebergs in the surrounding sea ice.

The spatial resolution of the AVE and SIR-reconstructed data is enhanced over that of conventional GRD processing. This is demonstrated in Fig. 5 for a synthetic $\sigma^\circ(x, y)$ scene and visually verified in Figs. 7 and 8 for ASCAT σ° measurement data. Other regions of the Earth similarly demonstrate enhanced resolution.

VI. Reconstruction Statistics

To quantify the performance of the reconstruction algorithms, the reconstructed data are characterized by first- and second-order statistics: the mean and variance of each pixel and the autocovariance between each pair of pixels. These statistics are used to evaluate the accuracy and precision of the reconstruction algorithms as applied to ASCAT.

For GRD and AVE, we predict the mean σ° for each pixel j and the autocovariance between pixels m and n. The mean is the expected value of the pixel

$$\mu_{\text{ave}}[j] = E\left[\sigma^\circ_{\text{ave}}[j]\right] \tag{15}$$

and the autocovariance is

$$k_{\text{ave}}(m, n) = E\left[\left(\sigma^\circ_{\text{ave}}[m] - \mu_{\text{ave}}[m]\right)\left(\sigma^\circ_{\text{ave}}[n] - \mu_{\text{ave}}[n]\right)\right]. \tag{16}$$

Due to the nonlinear nature of the SIR algorithm, the pixel mean and autocovariance are not readily computable, so instead, we use the sample mean and sample autocovariance through simulation. The sample statistics are computed for AVE and GRD and compared against the predicted values in order to validate the prediction. To simplify the analysis, no incidence angle dependence is included.

The simulation process includes two modeled sources of randomness: measurement noise and the uncertainty of the true Earth surface $\sigma^\circ(x, y)$. These effects are examined separately in Section VI-A and B, respectively. Signal and noise uncertainty are included together in Section VI-C. The resulting pixel statistics are used to compare the GRD, AVE, and SIR reconstruction methods. Section VI-D extends the pixel statistics analysis by examining the spectra of the images. Section VI-E summarizes the observations of this section.

A. Measurement Noise

As stated earlier in (13), the multiplicative measurement noise model is

$$z_i = \sigma^\circ_{\text{meas},i}(1 + K_{p,i}\,\nu_i) \tag{17}$$

where $\sigma^\circ_{\text{meas},i}$ is the sampled backscatter value, z_i is the noisy measurement, $K_{p,i}$ is a per-measurement noise term, and ν_i is a correlated Gaussian random process with zero mean and unit variance. For ASCAT, we treat $K_{p,i}$ as constant across the measurements so that $K_{p,i} = K_p$.

Substituting (13) into the AVE algorithm, (2), and taking the expectation over ν_i, the mean of $\sigma^\circ_{\text{ave}}$ for pixel m is

$$\mu_{\text{ave}}[m] = \frac{\sum_i \sigma^\circ_{\text{meas},i} h_{im}}{\sum_i h_{im}} \tag{18}$$

and the AVE autocovariance, noting that $E[\nu_i] = 0$ and $E[\nu_l \nu_k] = \delta_{lk}$, is

$$k_{\text{ave}}(m, n) = \frac{{K_p}^2 \sum_l \left(\sigma^\circ_{\text{meas},l}\right)^2 h_{lm} h_{ln}}{\sum_l h_{lm} \sum_k h_{kn}} \tag{19}$$

where i, l, and k index over the measurements and h_{ij} is the SRF value of measurement i at pixel j.

The mean and autocovariance for GRD are similar, but h_{ij} is replaced with the GRD indicator function G_{ij}. Noting that $\sum_i G_{ij} = N_j$ and $\sum_i G_{im} G_{in} = N_m \delta_{mn}$

$$\mu_{\text{grd}}[m] = \frac{\sum_i \sigma^\circ_{\text{meas},i} G_{im}}{N_m} \tag{20}$$

$$k_{\text{grd}}(m, n) = \begin{cases} \frac{{K_p}^2 \sum_l \left(\sigma^\circ_{\text{meas},l} G_{lm}\right)^2}{(N_m)^2}, & m = n \\ 0, & m \neq n. \end{cases} \tag{21}$$

Because GRD pixels do not share measurements with other pixels, the autocovariance of GRD pixels—due only to measurement noise—is 0 when $m \neq n$.

B. True Signal Uncertainty

The true image $A[j] = \sigma^\circ[x, y]$ is modeled as having first- and second-order statistics $\mu_A[j]$ and $k_A(m, n)$, the mean at pixel j, and autocovariance between pixels m and n, respectively. Neglecting measurement noise, the discretized sampling process is

$$z_i = \frac{\sum_j A[j] h_{ij}}{\sum_j h_{ij}}. \tag{22}$$

The mean and autocovariance of the measurements are

$$\mu_z[i] = \frac{\sum_j \mu_A[j] h_{ij}}{\sum_j h_{ij}} \tag{23}$$

$$k_z(a, b) = \frac{\sum_m \sum_n k_A(m, n) h_{am} h_{bn}}{(\sum_m h_{am})(\sum_n h_{bn})} \tag{24}$$

where j, m, and n index the pixels.

Using the AVE algorithm from (2), the mean for each pixel j and the autocovariance between the pixels m and n are

$$\mu_{\text{ave}}[j] = \frac{\sum_a \mu_z[a] h_{aj}}{\sum_a h_{aj}} \tag{25}$$

$$k_{\text{ave}}(m, n) = \frac{\sum_a \sum_b k_z(a, b) h_{am} h_{bn}}{\sum_a h_{am} \sum_b h_{bn}} \tag{26}$$

where a and b index the measurements.

For the GRD method, the indicator G_{ij} replaces the SRF value h_{ij} and $\sum_i G_{ij} = N_j$ is the number of measurements falling within each GRD pixel j. The GRD mean and autocovariance are therefore

$$\mu_{\text{grd}}[j] = \frac{1}{N_j} \sum_a \mu_z[a] G_{aj} \tag{27}$$

$$k_{\text{grd}}(m, n) = \frac{1}{N_m N_n} \sum_a \sum_b k_z(a, b) G_{am} G_{bn} \tag{28}$$

where a and b index over the measurements. Unlike the measurement noise case in (21), the GRD autocovariance is not necessarily a delta function but is a function of the truth image autocovariance $k_A(m, n)$.

C. Signal and Noise Uncertainty

Including both measurement noise and a stochastic signal from the preceding subsections, the measurements from (17) are replaced with the measurement mean and autocovariance

$$\mu_z[i] = \frac{\sum_j \mu_A[j] h_{ij}}{\sum_j h_{ij}} \tag{29}$$

$$\begin{aligned} k_z(a, b) = {} & \frac{\sum_k \sum_l k_A(k, l) h_{ak} h_{bl}}{\sum_k h_{ak} \sum_l h_{bl}} + {K_p}^2 \delta_{ab} \\ & \cdot \frac{\sum_k \sum_l \left(k_A(k, l) + \mu_A[k] \mu_A[l]\right) h_{ak} h_{bl}}{\sum_k h_{ak} \sum_l h_{bl}}. \end{aligned} \tag{30}$$

The measurement noise ν_i is assumed uncorrelated with the truth image, so $E[A[j]\nu_i] = E[A[j]]E[\nu_i] = 0$. With noise included, the measurement mean μ_z is unchanged from (23), but the measurement autocorrelation k_z has an additional term. Because of the Kronecker delta δ_{ab}, the second term only is nonzero when computing the variance of measurement z_a. This implies that the covariance between measurements $a \neq b$ is unaffected by measurement noise. However, with measurement noise, the measurement variance increases. The mean and autocovariance of the reconstructed pixels may be found by substituting the measurement statistics of (29) and (30) into (25) and (26) for AVE and (27) and (28) for GRD.

Simulation is used to validate the predicted GRD and AVE statistics. Synthetic truth images are created, sampled with the ASCAT measurement geometry and SRF, and then reconstructed using GRD, AVE, and SIR.

To create the truth images, a mean vector and an autocovariance matrix, μ_A and Σ_A, are generated. A multivariate Gaussian distribution is used with the parameters μ_A and Σ_A to obtain multiple realizations of truth images. The truth images are sampled with the SRF and the ASCAT measurement geometry over an equatorial region using 5 days of data. Noise is added to the measurements using (13) with a constant K_p value of 0.20. The truth images and sampling geometry are additionally used to compute the measurement statistics of (29) and (30). Equations (25) to (28) are used to predict the AVE and GRD pixel statistics.

In addition to the predicted statistics, the statistics are also measured from the simulation realizations. From the noisy measurements, the GRD, AVE, and SIR algorithms reconstruct the output image. The reconstructed images are created for each signal/noise realization; for the following results, 500 realizations of signal/noise are generated, so 500 sets of GRD/AVE/SIR images are created. The sample mean and sample autocovariance are taken over the realizations, computed independently for each image pixel.

A subset of the sample pixel mean and variance are shown in Fig. 9 for GRD, AVE, and SIR. For GRD, a grid spacing at both 12.5 and 25 km is used. AVE and SIR are both computed on a grid spacing of 3.125 km. For comparison, the GRD pixels are upsampled appropriately to match the AVE/SIR pixel size. The pixel mean subplot of Fig. 9 additionally includes the truth image mean. GRD and AVE are centered around the truth image mean, but SIR has a slight bias of -0.025 dB.

The pixel variance in Fig. 9 is typically largest for GRD at 12.5 km, is generally less for AVE, and is still less for SIR, and GRD at 25 km has the lowest pixel variance. As predicted, the pixel variance decreases for GRD and AVE as the number of measurements used to compute each reconstructed pixel increases. The number of measurements per pixel is shown in the bottom subplot of Fig. 9 for GRD and AVE (SIR has the same number of measurements per pixel as does AVE). Even though SIR uses the same number of measurements per pixel as does AVE, the pixel variance is lower for SIR than for AVE. Although not shown, the predicted AVE and GRD pixel mean and variance match the sample mean and variance within the error bounds predicted by using a finite sample size.

The autocovariance among pixel pairs is next evaluated. To increase the clarity of the plots, the correlation coefficient is plotted rather than the autocovariance. The correlation coefficient ranges between ±1

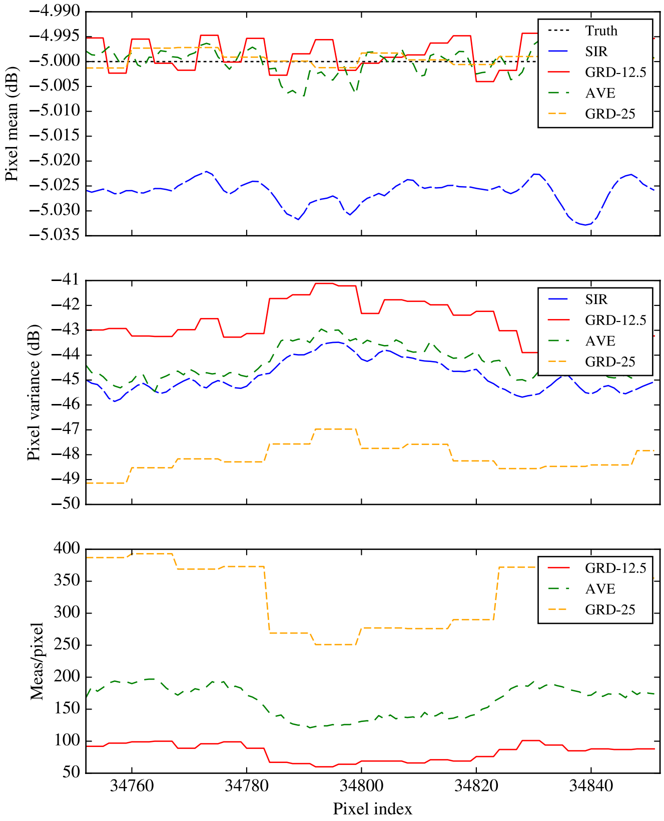

Fig. 9. (Top) Sample mean and (middle) variance for a few pixels of GRD, AVE, and SIR. GRD is computed on a grid spacing of both 25 and 12.5 km. AVE and SIR are on a grid spacing of 3.125 km. The number of measurements used to compute each pixel (bottom) is shown for the three grid spacings.

$$\rho(m,n) = \frac{k(m,n)}{\sqrt{k(m,m)\,k(n,n)}}. \tag{31}$$

For the purposes of this paper, we define the *correlation area* as the area in the correlation neighborhood covered by the contour 3 dB below the peak value of 1 and the *correlation length* as the radius of the 3-dB correlation contour.

The autocovariance $k(m,n)$, and therefore correlation coefficient $\rho(m,n)$, varies as a function of position due to the ASCAT sample geometry, including the SRF shape and orientation. The exact values differ as a function of location, but we observe that the general behavior is consistent over the image. For an example pixel from GRD (both 25- and 12.5-km grid spacings), AVE, and SIR, the sample correlation coefficient $\rho(m,n)$ between the pixel and its neighboring pixels is shown in Fig. 10. The GRD pixels are upsampled to match the area in the AVE and SIR cases.

In Fig. 10, both GRD-25 and GRD-12.5 have a very small correlation between neighboring pixels; however, since the grid spacing is large, the resulting correlation area is also large. The correlation area for AVE is about the same as for GRD-12.5, whereas SIR increases the correlation area beyond that of AVE. (For the pixels used in Fig. 10, the correlation areas for GRD-12.5, GRD-25, AVE, and SIR are 634, 158, 175, and

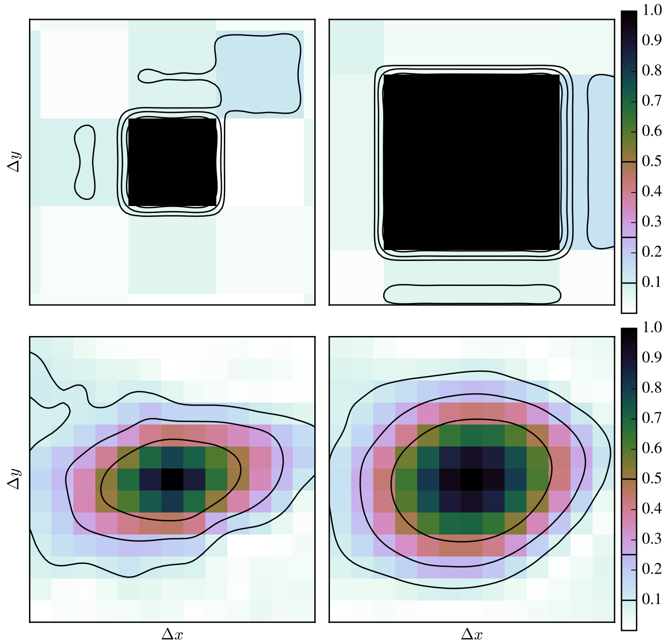

Fig. 10. Correlation coefficient between a random pixel and its neighboring pixels for (top left) GRD at a grid of spacing of 12.5 km, (top right) GRD on a spacing of 25 km, (bottom left) AVE at a spacing of 3.125 km, and (bottom right) SIR (30 iterations) at a spacing of 3.125 km. The GRD pixels are upsampled to match the AVE/SIR grid spacing. Contours are drawn at -3, -6, and -10 dB.

314 km^2, respectively). However, due to the measurement geometry and SRF shape, AVE typically has irregularly shaped correlation contours, while SIR smooths the contours to be more circularly symmetric, i.e., the variance of the correlation length is smaller for SIR than for AVE.

A desirable correlation coefficient area is small (so pixels are only weakly correlated with adjacent pixels) but symmetric (so the correlation distance is directionally isotropic). GRD satisfies both these conditions, but the grid spacing is large. AVE provides a smaller correlation area than GRD, but it is less symmetric than GRD. SIR tends to improve the correlation symmetry of AVE at the tradeoff of a larger correlation area.

D. Spectral Analysis

Due to measurement spacing and SRF size and orientation, the effective resolution of the reconstructed images may vary across the image. It is therefore difficult to precisely quantify the resolution of the reconstructed images as a single value. However, in order to determine an approximate effective resolution, we conduct a basic spectral analysis on the reconstructed images.

The synthetic truth image used is shown in Fig. 11. It contains a linear frequency-modulated chirp in order to test a wide range of spatial frequencies. In order to considerably simplify the analysis, the same 1-D values are used for each row of the synthetic truth image. The synthetic chirp image is treated as deterministic, so the only uncertainty is the added measurement noise. Using an (essentially) 1-D truth image permits simplifying the image spectrum to 1-D as well. The image spectrum, as used here, is the row-wise power spectrum computed using Welch's method.

Fig. 11. Chirp truth image used for spectral analysis.

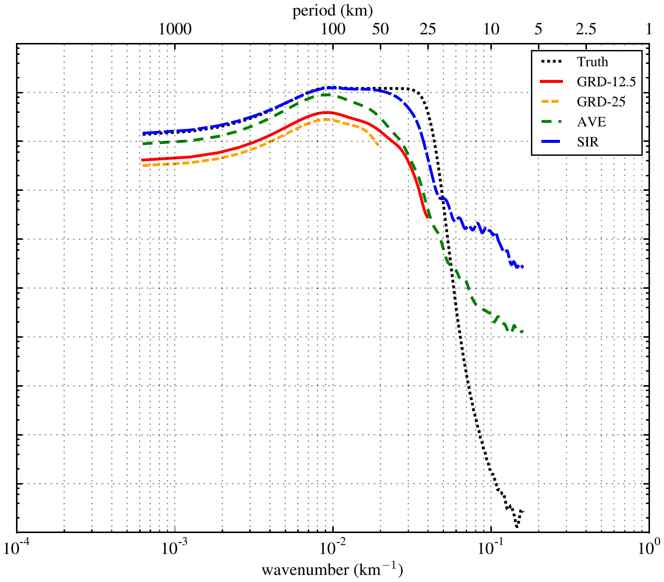

Fig. 12. Spectra for GRD, AVE, and SIR. The spectrum of the truth chirp image is shown for comparison. For clarity, the GRD spectra are plotted shifted downward slightly but otherwise are very similar to the AVE spectrum. GRD is computed on grid spacings of 12.5 and 25 km, and AVE and SIR are on a grid spacing of 3.125 km.

The spectra for GRD, AVE, and SIR are shown in Fig. 12. As before, grid spacings of 12.5 and 25 km are used for GRD and a grid spacing of 3.125 km is used for AVE and SIR; additionally, the ASCAT measurement geometry is from an equatorial region using 5 days of data. The spectra of the reconstructed outputs follow the behavior of the truth spectrum down to a wavenumber of about 0.01 km^{-1} (a spatial period of 100 km). Below that, AVE and GRD have similar values, but the spectra taper off. This is effectively a nonideal low-pass filtering of the truth image. The AVE spectrum continues to decrease until high-frequency noise starts to dominate below a wavenumber of about 0.05 km^{-1} (20 km).

Although the GRD pixel resolutions for the two cases considered in this paper are 25 and 50 km, the effective resolution of GRD is somewhat more coarse than this. This is due to the SRF of each measurement not always being entirely contained in the same pixel as the measurement center. This is evident in the falling off of the GRD power spectra in Fig. 12 below 100 km.

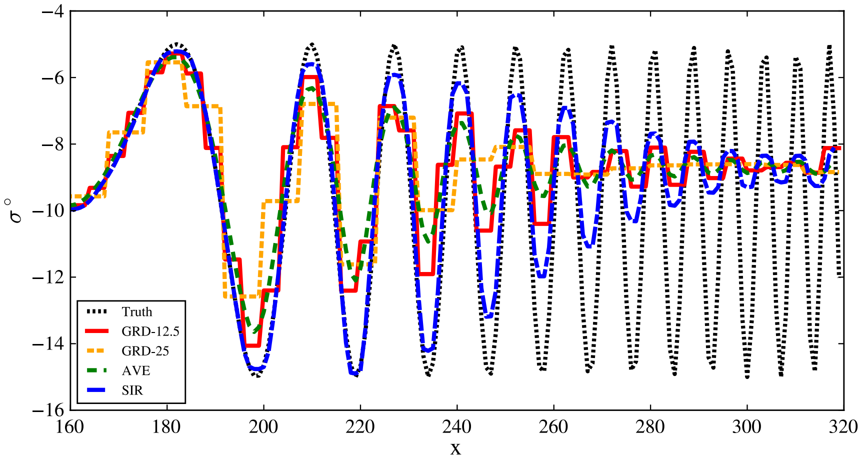

Fig. 13. Averaged row values for the truth input and the GRD, AVE, and SIR outputs. Due to symmetry, only half of the row is shown.

The SIR spectrum in Fig. 12 is similar to AVE, but it successfully recovers more frequency content between wavenumbers of 0.01 km^{-1} to 0.05 km^{-1} than AVE or GRD. Similar to AVE, below about 0.05 km^{-1}, the spectrum values are larger than the truth spectrum, and the slope of the spectrum is more shallow, indicating that high-frequency noise dominates.

Fig. 13 shows the spatial domain results, or the values of the rows of the images averaged together. Since the image is symmetric, only half of the averaged row is shown. For all reconstruction cases considered, the recovered amplitude decays as frequency increases, in agreement with the spectrum results in Fig. 12. GRD cannot recover the highest frequencies due to aliasing. AVE and SIR recover all the frequencies for this particular chirp, but with diminished amplitudes. SIR, however, is able to recover the amplitudes better than AVE, particularly the troughs of each wave. The improved amplitude recovery of SIR versus GRD and AVE matches the higher energy in midrange frequencies in Fig. 12.

The spectra are also computed using ASCAT measurement geometry from a polar region. Due to the near-polar orbit of ASCAT, a high-latitude region is more densely sampled than at lower latitudes: i.e., the δ-density value is smaller. With 5 days of data, the spectra (not shown) indicate an effective resolution of 12.5 km. However, in order to improve the temporal resolution of polar regions (e.g., to detect and track fast-moving icebergs), 2 days of ASCAT data are used. The spectra for 2-day polar regions indicate a spatial resolution of about 15 km.

Including data from both ASCAT instruments on MetOp-A and MetOp-B together in tandem processing further increases the number of measurements. The spectrum results (not shown) do not support an improved spatial resolution—this is likely due to the two MetOp satellites operating in a coplanar orbit. However, tandem processing enables improved temporal resolution since combining data from both instruments improves the coverage over that using only a single ASCAT instrument.

Although the spectrum results vary as a function of parameters, the truth image, and the measurement geometry, the general trends observed are similar. The results in both spatial and frequency domains show that both AVE and SIR contain spatial content down to about 15 km but, as evidenced by the attenuation, cannot recover *all* data to 15 km. However, SIR has less attenuation and is better able than AVE to recover the high-frequency content.

E. Summary

This section has evaluated the GRD, AVE, and SIR methods by comparing the pixel mean, pixel variance, and correlation neighborhoods and by a spectral analysis. Although the pixel statistics may be predicted for GRD and AVE, in order to additionally consider SIR, the sampling process is simulated, and the measured statistics are compared. As mentioned previously, because the number of SIR iterations is truncated, it is a partial reconstruction approach.

For the cases considered here, GRD and AVE both are unbiased, while SIR exhibits a small bias. SIR, however, improves the pixel variance over AVE. The pixel variance of GRD depends on the grid spacing, which affects the number of measurements used for each GRD pixel. For the two cases examined (12.5 and 25 km), the GRD pixel variance is either greater than or less than that of AVE and SIR.

GRD pixels are weakly correlated with neighboring pixels, but AVE and SIR have a larger number of adjacent pixels correlated. AVE has a small correlation area, but the correlation is typically nonsymmetric. SIR improves the correlation symmetry but at the tradeoff of a larger correlation area.

The coarse grid spacing of GRD precludes the recovery of high spatial frequencies. AVE and SIR are both able to recover content down to a scale of about 15 km, but with some attenuation. SIR improves the frequency recovery over AVE with higher amplitude recovered frequencies. Both AVE and SIR provide improved spatial resolution over GRD.

VII. CONCLUSION

Image reconstruction algorithms in conjunction with the measurement SRF enable enhanced-resolution estimates of the sampled Earth surface σ°. The effective spatial resolution of the reconstructed AVE and SIR products is difficult to precisely quantify for ASCAT but is on the order of 15 to 20 km compared to at least 25 km for GRD-12.5 and 50 km for GRD-25. Increasing the number of ASCAT passes used increases the sample density, which also improves the resolution (to a point) and reduces noise.

The parameters of reconstruction discussed include the choice of pixel size, quantizing the measurement SRF, and the number of SIR iterations. We choose a pixel size of 4.45 km/pixel for compatibility with other products in the SCP data set. This is selected to balance the requirements of using a pixel resolution finer than the effective resolution but not so fine as to provide no additional benefit for the larger storage requirement. Based on simulated truth images and actual observation geometry, we select 30 iterations of SIR and do not use a quantized SRF. The choice of SIR iterations is a reasonable tradeoff to reduce signal error without needlessly amplifying reconstruction noise.

We also evaluate the pixel statistics of the GRD, AVE, and SIR methods, noting that the statistics are dependent on the SRF and sample geometry. Here, we examine the results for ASCAT, but the techniques may be readily applied for any arbitrary SRF and sample geometry, e.g., for another scatterometer. We find that SIR introduces a small bias of about 0.02 dB but has a lower pixel variance than AVE. The pixel variance of GRD is directly proportional to the number of measurements used per pixel; thus, the choice of grid spacing is an important consideration for GRD. However, the number of measurements per pixel for AVE and SIR is affected by the sampling geometry and measurement SRF, not the grid spacing; thus, the grid spacing size is not significant for AVE and SIR pixel variance.

The correlation coefficient between reconstructed pixel pairs is also evaluated. GRD pixels are only weakly correlated with adjacent pixels, but the correlation extends further for AVE and SIR. Because of the measurement geometry and SRF shape, the correlation coefficient may be directionally dependent for AVE. SIR, however, tends to circularize the correlation coefficient contours at the tradeoff of an increased correlation area.

A basic spectral analysis indicates that AVE and SIR perform a limited recovery of high-resolution information. The resolution recovery for GRD is constrained by the coarse grid spacing. SIR improves upon AVE and amplifies high-frequency content that is otherwise attenuated. Since the number of SIR iterations is truncated, it is only a partial reconstruction. Increasing the number of SIR iterations may continue to recover high-frequency content, but high-frequency noise is amplified as well.

The processed ASCAT σ° products at conventional resolution using GRD and at enhanced resolution using AVE and SIR are publicly available in the SCP archives (http://scp.byu.edu), and we anticipate their use in a variety of geoscience applications.

REFERENCES

[1] R. D. Lindsley and D. G. Long, “Mapping surface oil extent from the Deepwater Horizon oil spill using ASCAT backscatter,” *IEEE Trans. Geosci. Remote Sens.*, vol. 50, no. 7, pp. 2534–2541, Jul. 2012.

[2] A. D. Fraser, N. W. Young, and N. Adams, “Comparison of microwave backscatter anisotropy parameterizations of the Antarctic ice sheet using ASCAT,” *IEEE Trans. Geosci. Remote Sens.*, vol. 52, no. 3, pp. 1583–1595, Mar. 2014.

[3] L. Breivik, S. Eastwood, and T. Lavergne, “Use of C-band scatterometer for sea ice edge identification,” *IEEE Trans. Geosci. Remote Sens.*, vol. 50, no. 7, pp. 2669–2677, Jul. 2012.

[4] W. Wagner *et al.*, “The ASCAT soil moisture product: A review of its specifications, validation results, and emerging applications,” *Meteorologische Zeitschrift*, vol. 22, no. 1, pp. 5–33, Feb. 2013.

[5] J. Figa-Saldaña *et al.*, “The Advanced Scatterometer (ASCAT) on the Meteorological Operational (MetOp) platform: A follow on for European wind scatterometers,” *Can. J. Remote Sens.*, vol. 28, no. 3, pp. 404–412, 2002.

[6] M. P. Owen and D. G. Long, “Towards an improved wind and rain backscatter model for ASCAT,” in *Proc. IEEE IGARSS*, Jul. 2010, pp. 2531–2534.

[7] D. S. Early and D. G. Long, “Image reconstruction and enhanced resolution imaging from irregular samples,” *IEEE Trans. Geosci. Remote Sens.*, vol. 39, no. 2, pp. 291–302, Feb. 2001.

[8] J. P. Bradley and D. G. Long, “Estimation of the OSCAT spatial response function using island targets,” *IEEE Trans. Geosci. Remote Sens.*, vol. 52, no. 4, pp. 1924–1934, Apr. 2014.

[9] D. G. Long, “NSCAT views land and ice,” in *Proc. IEEE IGARSS*, 1998, vol. 4, pp. 1973–1975.

[10] A. M. Swan and D. G. Long, “Multiyear Arctic sea ice classification using QuikSCAT,” *IEEE Trans. Geosci. Remote Sens.*, vol. 50, no. 9, pp. 3317–3326, Sep. 2012.

[11] Q. P. Remund and D. G. Long, “A decade of QuikSCAT scatterometer sea ice extent data,” *IEEE Trans. Geosci. Remote Sens.*, vol. 52, no. 7, pp. 4281–4290, Jul. 2014.

[12] L. B. Kunz and D. G. Long, “Melt detection in Antarctic ice shelves using scatterometers and microwave radiometers,” *IEEE Trans. Geosci. Remote Sens.*, vol. 44, no. 9, pp. 2461–2469, Sep. 2006.

[13] K. M. Stuart and D. G. Long, “Tracking large tabular icebergs using the SeaWinds Ku-band microwave scatterometer,” *Deep Sea Res. II, Top. Stud. Oceanogr.*, vol. 58, no. 11/12, pp. 1285–1300, Jun. 2011.

[14] K. M. Stuart and D. G. Long, “Iceberg size and orientation estimation using SeaWinds,” *Cold Regions Sci. Technol.*, vol. 69, no. 1, pp. 39–51, Jul. 2011.

[15] S. Frolking, M. Fahnestock, T. Milliman, K. McDonald, and J. Kimball, “Interannual variability in North American grassland biomass/productivity detected by SeaWinds scatterometer backscatter,” *Geophys. Res. Lett.*, vol. 32, no. 21, 2005, Art. ID L21409.

[16] S. R. Oza, S. Panigrahy, and J. S. Parihar, “Concurrent use of active and passive microwave remote sensing data for monitoring of rice crop,” *Int. J. Appl. Earth Observ. Geoinf.*, vol. 10, no. 3, pp. 296–304, Sep. 2008.

[17] B. A. Williams, M. P. Owen, and D. G. Long, “The ultra high resolution QuikSCAT product,” in *Proc. IEEE Radar Conf.*, May 2009, pp. 1–6.

[18] F. Saïd and D. G. Long, “Determining selected tropical cyclone characteristics using QuikSCAT’s ultra-high resolution images,” *IEEE J. Sel. Topics Appl. Earth Observ. Remote Sens.*, vol. 4, no. 4, pp. 857–869, Dec. 2011.

[19] I. S. Ashcraft and D. G. Long, “The spatial response function of SeaWinds backscatter measurements,” in *Proc. SPIE: Earth Observ. Syst. VIII*, W. L. Barnes, Ed., Aug. 3–6, 2003, vol. 5151, pp. 1–10.

[20] D. G. Long, P. Hardin, and P. Whiting, “Resolution enhancement of spaceborne scatterometer data,” *IEEE Trans. Geosci. Remote Sens.*, vol. 31, no. 3, pp. 700–715, May 1993.

[21] B. A. Williams and D. G. Long, “Reconstruction from aperture-filtered samples with application to scatterometer image reconstruction,” *IEEE Trans. Geosci. Remote Sens.*, vol. 49, no. 5, pp. 1663–1676, May 2011.

[22] R. D. Lindsley, C. Anderson, J. Figa-Saldaña, and D. G. Long, “A parameterized ASCAT measurement spatial response function,” *IEEE Trans. Geosci. Remote Sens.*, to be published.

[23] R. D. Lindsley, J. R. Blodgett, and D. G. Long, “Analysis and validation of high-resolution wind from ASCAT,” *IEEE Trans. Geosci. Remote Sens.*, to be published.

[24] G. E. Backus and J. F. Gilbert, “Numerical applications of a formalism for geophysical inverse problems,” *Geophys. J. Int.*, vol. 13, no. 1–3, pp. 247–276, Jul. 1967.

[25] D. G. Long and D. L. Daum, “Spatial resolution enhancement of SSM/I data,” *IEEE Trans. Geosci. Remote Sens.*, vol. 36, no. 2, pp. 407–417, Mar. 1998.

[26] F. Lenti, F. Nunziata, C. Estatico, and M. Migliaccio, “On the spatial resolution enhancement of microwave radiometer data in Banach spaces,” *IEEE Trans. Geosci. Remote Sens.*, vol. 52, no. 3, pp. 1834–1842, Mar. 2014.

[27] D. G. Long, M. R. Drinkwater, B. Holt, S. Saatchi, and C. Bertoia, “Global ice and land climate studies using scatterometer image data,” *EOS Trans., Amer. Geophys. Union*, vol. 82, no. 43, p. 503, Oct. 2001.

[28] R. D. Lindsley and D. G. Long, “Standard BYU ASCAT Land/Ice Image Products,” Brigham Young Univ. (BYU) Microw. Earth Remote Sens. (MERS) Lab., Provo. UT, USA, Tech. Rep., 2010. [Online]. Available: http://www.mers.byu.edu/docs/reports/MERS1002.pdf

[29] I. Birrer, E. Bracalente, G. Dome, J. Sweet, and G. Berthold, “σ° signature of the Amazon rain forest obtained from the Seasat scatterometer,” *IEEE Trans. Geosci. Remote Sens.*, vol. GE-20, no. 1, pp. 11–17, Jan. 1982.

[30] R. D. Lindsley and D. G. Long, “Adapting the SIR algorithm to ASCAT,” in *Proc. IEEE IGARSS*, 2010, pp. 3402–3405.

[31] K. Gröchenig, “Reconstruction algorithms in irregular sampling,” *Math. Comput.*, vol. 59, no. 199, pp. 181–194, Jul. 1992.

[32] “Estimation of ASCAT-normalised radar cross section: ATBD,” Europäische Organisation für Meteorologische Satelliten (EUMETSAT), Darmstadt, Germany, Ref. EUM/TSS/SPE/14/762689, Jul. 2014.

[33] P. K. Yoho and D. G. Long, “An improved simulation model for spaceborne scatterometer measurements,” *IEEE Trans. Geosci. Remote Sens.*, vol. 41, no. 11, pp. 2692–2695, Nov. 2003.

Richard D. Lindsley (S’08) received the Ph.D. degree in electrical engineering from Brigham Young University (BYU), Provo, UT, USA, in 2015.

He has been with the Microwave Earth Remote Sensing Laboratory, BYU, since 2008. His research interests include microwave remote sensing and signal processing.

David G. Long (S’80–SM’98–F’08) received the Ph.D. degree in electrical engineering from the University of Southern California, Los Angeles, CA, USA, in 1989.

From 1983 to 1990, he worked for NASA’s Jet Propulsion Laboratory (JPL) where he developed advanced radar remote sensing systems. While at JPL, he was the Project Engineer on the NASA Scatterometer project which flew from 1996 to 1997. He also managed the SCANSCAT project, the precursor to SeaWinds which was flown in 1999 on QuikSCAT, in 2002 on ADEOS-II and in 2014 on the International Space Station. He is currently a Professor in the Electrical and Computer Engineering Department at Brigham Young University (BYU), Provo, UT, USA, where he teaches upper division and graduate courses in communications, microwave remote sensing, radar, and signal processing and is the Director of the BYU Center for Remote Sensing. He is the Principal Investigator on several NASA-sponsored research projects in remote sensing. He has over 400 publications in various areas, including signal processing, radar scatterometry, and synthetic aperture radar. His research interests include microwave remote sensing, radar theory, space-based sensing, estimation theory, signal processing, and mesoscale atmospheric dynamics.

Dr. Long has received the NASA Certificate of Recognition several times and is an Associate Editor for the *IEEE Geoscience and Remote Sensing Letters*.